Bioactive Materials 12 (2022) 143–152

Contents lists available at ScienceDirect

Bioactive Materials

journal homepage: www.keaipublishing.com/en/journals/bioactive-materials

Platinum–copper alloy nanoparticles armored with chloride ion transporter to promote electro-driven tumor inhibition

Tong Chen [a], Gaorong Han [a], Xiang Li [a,b,*]

[a] State Key Laboratory of Silicon Materials, School of Materials Science and Engineering, Zhejiang University, Hangzhou, Zhejiang, 310027, China
[b] ZJU-Hangzhou Global Scientific and Technological Innovation Centre, Zhejiang University, Hangzhou, 311200, PR China

ARTICLE INFO

Keywords:
Electrodynamic therapy
Chloride ion transporter
Alloy nanoparticles

ABSTRACT

The induction of oxidative species, driven by oscillating electric field (E), has recently emerged as an effective approach for tumor inhibition, so-called electrodynamic therapy (EDT). While it offers a series of advantages attracting considerable attention, the fundamental mechanism and improvement strategies for EDT approach are being endeavored extensively with the aid of new material explorations. An interesting phenomenon observed in early studies is that the on-site concentration of chloride ion is highly favored for the induction of oxidative species and the efficacy of tumor inhibition. Following this discovery ignored previously, here for the first time, fine Pt/Cu alloy nanoparticles ($PtCu_3$ NPs) are integrated with chloride ion transporter (CIT) for EDT-based combinational therapy. In this system, while $PtCu_3$ NPs induce oxidative species under an electric field, it also effectively transforms endogenous H_2O_2 into •OH and consumes intracellular glutathione (GSH). More importantly, with the aid of CIT, $PtCu_3$-PEG@CIT NPs promote the intracellular concentration of chloride ion (Cl^-) by transporting extracellular Cl^-, facilitating the generation of oxidative species considerably. Meanwhile, CIT delivered intracellularly increases lysosomal pH, leading to the disruption of cellular autophagy and weakening the treatment resistance. In consequence, significant tumor inhibition is enabled both *in vitro* and in vivo, due to the combination of unique characteristics offered by $PtCu_3$-PEG@CIT.

1. Introduction

The induction of reactive oxidative species (ROS), driven by oscillating electric field, has recently emerged as an effective approach for tumor inhibition, namely electrodynamic therapy (EDT) [1–4]. Noble metal nanoparticles such as Pt nanoparticles have attracted wide attention due to its unique optical, magnetic, catalytic and other properties [5,6]. EDT is enabled by the unique ROS generation of platinum nanoparticles under electric field [1]. Compared with other ROS-based treatment methods, EDT presents various distinct advantages, such as the feasibility in remote control by electric field, independence with H_2O_2 and O_2, low side effects and so on. The proposed mechanism by simulation suggests that the H_2O molecules and Cl^- ions favorably absorb at the (111) surface of Pt. With the agitation of electric field, Faraday cage effect appears on Pt nanoparticles (Pt NPs). The H–O bond breaks in the presence of Cl^- ions, and •OH with high cytotoxicity forms. This implies that Cl^- ions play important roles in driving the water dissociation owing to the catalytic reactions of Pt nanoparticles. The promoted intracellular concentration of chloride ion may remarkably favor the ROS generation and thus the tumor inhibition during EDT.

In general, the intracellular concentration of chloride ion is 5–40 mM, lower than that outside cells (~120 mM) [7]. Therefore, one potential strategy to increase the intracellular Cl^- concentration is to transport Cl^- from the outer to the inner cells utilizing chloride ion transporter (CIT) [8]. Prodigiosin is one of small-molecule natural anion transporters [9,10], which can recept and transport HCl [11]. The effectiveness of prodigiosin has inspired the development of diverse artificial transporters [12]. The most common chloride transporter is mono-squaramide [13], which can promote Cl^- and Na^+ influx into cells. In addition, lysosomal pH is also related to the chloride content [14]. When the lysosomal chloride content is maintained at 80 mM, the lysosomal pH remains under 5.0 [15]. The reduction of lysosomal chloride content can cause the increase of lysosomal pH, and thus the activity of lysosomal is disrupted, leading to autophagy disruption [15].

Peer review under responsibility of KeAi Communications Co., Ltd.
* Corresponding author. State Key Laboratory of Silicon Materials, School of Materials Science and Engineering, Zhejiang University, Hangzhou, Zhejiang, 310027, China.
E-mail address: xiang.li@zju.edu.cn (X. Li).

https://doi.org/10.1016/j.bioactmat.2021.10.012
Received 21 June 2021; Received in revised form 6 October 2021; Accepted 8 October 2021
Available online 13 October 2021

In principle, autophagy is a cell self-feeding process, which protects cell from various therapeutics [16]. Recently, autophagy has been extensively studied for tumor therapy and other medical purposes such as COVID-19 treatment [17]. Therefore, in addition to its favorable role in the ROS induction, the cellular influx of Cl^- may also facilitate the tumor inhibition of EDT *via* the induction of autophagy disruption.

In addition to endeavoring to promote the on-site ROS induction, a common approach to facilitate cancer inhibition is to suppress the phenomenon of ROS scavenging by intracellular antioxidant system, i.e. glutathione (GSH) [18]. In fact, the depletion of GSH has been extensively adopted and combined with ROS-based therapies, and some strategies have been proposed. For instance, L-buthioninesulfoximine (BSO) can inhibit cellular GSH synthesis [19,20]. Meanwhile, the redox reactions based on metal ions, such as Mn^{4+} [21,22], Fe^{3+} [23,24], Cu^{2+} [25,26] and so on [27], have been utilized to convert the intracellular GSH to glutathione disulfde (GSSG) and to enable GSH depletion. Nonetheless, the integration of GSH depletion factors, such as drug molecules or metal oxides, at the surface of Pt nanoparticles can remarkably weaken the ROS induction and thus the EDT efficacy following the current knowledge for EDT phenomenon. A feasible approach to integrate the functionality of GSH depletion with current EDT agents, while maintaining its expected ROS induction, is of high demand, but remains challenging.

$PtCu_3$ alloy nanoparticles have recently been reported as the platform for sonodynamic therapy (SDT) [28]. This 'milestone' study revealed that the underlying mechanism of SDT induced by $PtCu_3$ nanoparticles is attributed to the oxidized Cu ions of $PtCu_3$-PEG. However, here in our study, the similar $PtCu_3$ nanoparticles, but with different functional mechanism and focus, was synthesized and combined with CIT molecules ($PtCu_3$-PEG@CIT NPs) as a potential platform enabling CIT amplified EDT (Fig. 1). In this system, the cubic $PtCu_3$ NPs modified with PEG ($PtCu_3$-PEG NPs) not only generate ROS under the electric field, but also play multiple roles as a Fenton-like reaction agent that can catalyze H_2O_2 to •OH and an agent that depletes intracellular GSH. More importantly, CIT loaded and delivered by $PtCu_3$-PEG@CIT NPs effectively increases intracellular chloride ion concentration and lysosomal pH, resulting in promoted ROS induction, clear autophagy disruption and the weakened therapeutic resistance of tumor cells. $PtCu_3$-PEG@CIT NPs enable significant effect in tumor inhibition under the oscillating electric field. This study appears to offer a distinctive concept in enhancing the antitumor efficacy of EDT following the current mechanistic understanding of this technology in cancer therapy.

2. Materials and methods

2.1. Chemical and reagents

Platinum acetylacetonate ($Pt(acac)_2$), oleylamine (OAM), cetyltrimethyl ammonium bromide (CTAB), copper acetylacetonate ($Cu(acac)_2$), N-2-hydroxyethylpiperazine-N′-2-ethanesulfonic acid (HEPES), zinc trifluoromethanesulfonate, N-Methyl-D-glucamine (NMDG) and D-glucose were obtained from Aladdin Industrial Co., Ltd. 3,4-Diethoxy-3-cyclobutene-1,2-dione were obtained from TCI Chemical Industry Co., Ltd. Methoxy polyethylene glycol mercapto (mPEG-SH, Mw = 5000), N,N-Dimethylformamide (DMF) and 4-(trifluoromethyl) aniline were obtained from Macklin Industrial Co., Ltd. Toluene, methanol, sodium chloride (NaCl), alcium chloride ($CaCl_2$), magnesium chloride ($MgCl_2$), potassium chloride (KCl) were obtained from Sinopharm Chemical Reagent Co., Ltd. Anti-rabbit LC3, anti-mouse p62 and mouse β-actin antibodies was obtained from Beyotime Biotechnology Co., Ltd. SBFI AM (Na^+ Indicator), MQAE (Cl^- indicator) were purchased from Sigma-Aldrich. Fluorescein-tetramethyl rhodamine-tagged dextran were obtained from Thermo Fisher Scientific Co., Ltd.

2.2. Synthesis $PtCu_3$-PEG@CIT

$PtCu_3$ NPs were synthesized by solvothermal process following the previous work with some improvement [29]. Briefly, 34.6 mg $Cu(acac)_2$

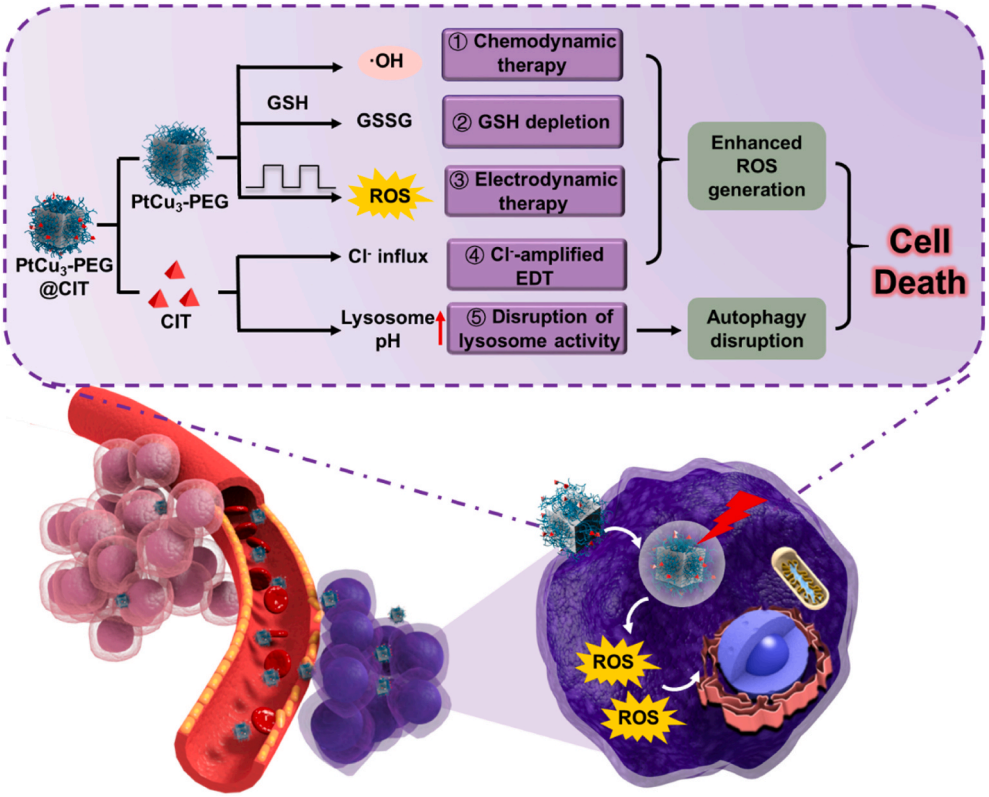

Fig. 1. Schematic illustration of functional characteristics of $PtCu_3$-PEG@CIT nanoparticles for EDT-based combinational therapy with promoted efficacy.

and 10.35 mg $Pt(acac)_2$ were put in 10 mL oleylamine. 175 mg CTAB was also put in 10 mL oleylamine. The CTAB solution was put into the above solution. Finally, the mix solution was transferred into reaction still and heated at 170 °C for 48 h. The $PtCu_3$ NPs was dispersed in acetone and centrifugated. The obtained $PtCu_3$ NPs were dispersed into 5 mL ethanol. Then, 50 μL HCl solution (10 M) were put into it. Then, reaction was sonicated for 0.5 h to remove oleylamine ligand on surface of $PtCu_3$ NPs. Then, oleylamine-free $PtCu_3$ NPs. were centrifugated and washed with acetone. 10 mg $PtCu_3$ NPs and 100 mg mPEG-SH were dispersed in 10 mL water and magnetically stirred for 24 h. Finally, the $PtCu_3$-PEG NPs were obtained by centrifugation.

CIT was synthesized following the method [13]. 0.5 g 3,4-Diethoxy-3-cyclobutene-1,2-dione and 210 mg zinc trifluoromethanesulfonate were dissolved in 19:1 toluene: DMF (5 mL). Next, 783 μL 4-(trifluoromethyl) aniline was put into above solution. The solution was heated overnight at 100 °C. After cooling, precipitates were filtered off and washed with methanol until filtrate appeared colorless. The resulting solid was dried in high vacuum for 24 h and CIT was obtained as a pale yellow solid.

Typically, $PtCu_3$-PEG and CIT were stirred for 12 h (CIT/$PtCu_3$ (w/w) = 0.8, 0.4, 0.2, 0.08, 0.04). Particularly, CIT was dissolve with DMSO, then diluted for 1000 times to add to the $PtCu_3$-PEG solution. Subsequently, the $PtCu_3$-PEG@CIT nanocomposite was centrifugated and washed to remove the unattached CIT. UV–vis spectroscopy was utilized to measure absorption spectra of $PtCu_3$-PEG@CIT NPs with the characteristic peak at 360 nm. According to the standard curve, the CIT loading amount on the $PtCu_3$-PEG NPs could be obtained. The loading capacity and the loading efficacy could be calculated by the following equation:

Loading capacity = (the quantity of CIT in $PtCu_3$-PEG / the quantity of $PtCu_3$-PEG) × 100%

Loading efficacy = (the quantity of CIT in $PtCu_3$-PEG)/ the quantity of added-CIT) × 100%

2.3. Fenton reaction activity studies

3,3′,5,5′-Tetramethylbenzidine (TMB) was used to evaluate Fenton reaction activity of $PtCu_3$-PEG NPs by the chromogenic reaction (λ = 652 nm). PBS (pH = 6) and 100 mM H_2O_2 was used. The steady-state kinetic catalytic activities of 100 μg/mL $PtCu_3$-PEG NPs were investigated by measuring absorbance variation at 652 nm upon addition of varied H_2O_2 concentration (10, 20, 30, 40 mM).

2.4. Depletion of GSH

10 mg $PtCu_3$-PEG NPs was put into 10 mL GSH solution (1 mM). After different times, 500 μL solution was taken out and centrifuged to remove $PtCu_3$-PEG NPs. And the supernatant was diluted six times. Next, 50 μL 5, 5′-dithiobis-(2-nitrobenzoic acid) (DTNB) (10 mM) was added. The absorbance spectra of the above solution were investigated by UV–vis spectroscopy.

2.5. Electro-catalytic activity studies

A common ROS probe, methylene blue (MB) was utilized to investigate electro-catalytic properties of $PtCu_3$-PEG NPs. 50 μL MB (1 mM) and different amount $PtCu_3$-PEG NPs was put into 2 mL PBS. The experiment equipment and parameters of electric field were the same as our previous work [2]. After different times, 50 μL solution was taken out and diluted four times and UV–vis spectroscopy was used to investigate absorption spectra of MB. The MB degradations abilities of $PtCu_3$-PEG NPs with different concentrations were studied. In addition, the MB degradation abilities of $PtCu_3$-PEG NPs with different chloride ion (0.05, 0.1, 0.25, 0.5, 1, 2 M) were studied.

2.6. In vitro studies

All the cell viabilities were evaluated by CCK-8 assay after incubated for 24 h. 1×10^4 7702 cells were plated in 96-well plate for 12 h. Then, different concentrations of $PtCu_3$-PEG NPs were added into cells.

4T1 breast tumor cells were used for the *in vitro* studies. For CDT treatment, medium (pH = 6) containing $PtCu_3$-PEG NPs at varied concentrations of 3, 6, 12, 25, 50 μg/mL for $PtCu_3$ containing 100 μM H_2O_2 were added into 4T1 cells. For EDT, 1×10^5 4T1 cells were seeded in 24-well plate and co-cultured with $PtCu_3$-PEG NPs or $PtCu_3$-PEG@CIT NPs at varied concentrations of 0, 3, 6, 12, 25, 50 μg/mL for $PtCu_3$ and 0, 0.6, 1.2, 2.4, 5, 10 μM for CIT for 4 h. Then, electric field (square wave, 10 mHz, 5 mA) was imposed to the cells for 3 min. For combined treatment, $PtCu_3$-PEG NPs at varied concentrations of 3, 6, 12, 25, 50 μg/mL for $PtCu_3$ containing 100 μM H_2O_2 were co-cultured with cells for 4 h, and exposed to E (square wave, 10 mHz, 5 mA) for 3 min.

For CDT and CIT enhanced EDT, 4T1 cells were co-cultured with $PtCu_3$-PEG@CIT at varied concentrations of 0, 3, 6, 12, 25, 50 μg/mL for $PtCu_3$, and 0, 0.6, 1.2, 2.4, 5, 10 μM for CIT containing 100 μM of H_2O_2 for 4 h, followed by exposing to the same E for the same time.

2.7. Sodium and chloride depletion study

HEPES-buffered solutions were prepared with the following compositions: 10 mM HEPES (pH 7.4), 10 mM D-glucose, 1 mM $CaCl_2$, 5 mM KCl, 120 mM NaCl, 1 mM $MgCl_2$, 25 mM $NaHCO_3$. To prepare Na^+–free or Cl^-–free HEPES-buffered solutions, Na^+ or Cl^- ions in buffer solutions were replaced with equimolar concentrations of respective NMDG.

4T1 Cells were co-cultured with 0–20 μM of CIT and $PtCu_3$-PEG@CIT (0–100 μg/mL for $PtCu_3$, 0–20 20 μM for CIT) in HEPES solutions, Na^+–free or Cl^-–free HEPES solutions.

2.8. Intracellular ROS generation

4T1 cells were applied to different operations including PBS, E (10 mHz, 5 mA, 3 min), $PtCu_3$-PEG (50 μg/mL for $PtCu_3$), $PtCu_3$-PEG + H_2O_2 (100 μM), $PtCu_3$-PEG + E, $PtCu_3$-PEG@CIT + E (50 μg/mL for $PtCu_3$, 10 μM for CIT), $PtCu_3$-PEG + H_2O_2 + E and $PtCu_3$-PEG@CIT + H_2O_2 + E and stained with 20 μM DCFH-DA and 1 μg/mL DAPI. The fluorescence images were obtained by fluorescence microscope.

2.9. Intracellular GSH content

The 4T1 cells were co-cultured with $PtCu_3$-PEG NPs at varied concentrations. Then, 200 μL lysis buffer was put into cells. After 10 min, the cells were collected and centrifugated. 50 μL DTNB solution (0.4 mM) was added into the supernate. After 30 min, the microplate reader was utilized to investigate absorbance of mixture at 412 nm.

2.10. Measurement of intracellular Cl^- concentrations

4T1 cells were co-cultured with $PtCu_3$-PEG@CIT (100 μg/mL for $PtCu_3$, 20 μM for CIT) for 0, 2, 4, 6 h or $PtCu_3$-PEG@CIT at varied concentrations (0, 12, 25, 50, 100 μg/mL for $PtCu_3$, 0, 2.4, 5, 10, 20 μM for CIT) for 6 h. Then, 10 mM MQAE was put into the cells and co-cultured for 30 min. The MQAE fluorescence was imaged by fluorescence microscope.

2.11. Measurement of intracellular Na^+ concentrations

4T1 cells were co-cultured with $PtCu_3$-PEG@CIT (100 μg/mL for $PtCu_3$, 20 μM for CIT) for 0, 2, 4, 6 h or $PtCu_3$-PEG@CIT at varied concentrations (0, 12, 25, 50, 100 μg/mL for $PtCu_3$, 0, 2.4, 5, 10, 20 μM for CIT) for 6 h. Then, 10 μM SBFI-AM containing 0.04% Pluronic F-127

was added into the cells and co-cultured for 30 min. The SBFI-AM fluorescence was imaged by a fluorescence microscope.

2.12. Western blot assay

The different samples were co-cultured with 4T1 cells for 4 h and exposed to square-wave AC treatment (10 mHz, 5 mA, 3 min). After 12 h, 200 μL lysis buffer was put into cells and the solution was centrifuged. Then, the SDS buffer was put into the supernatant and boiled for 5 min. Next, 12% SDS-PAGE was used to separate the samples. After transferring to the PVDF membrane, the samples were co-cultured with anti-LC3 and anti-Actin antibody overnight at 4 °C. Subsequently, the samples were co-cultured with a secondary antibody for 1 h. Finally, Bio-Rad chemoluminescence imaging system was used to measure the bands.

2.13. Measurement of lysosomal pH

4T1 cells were treated with 1 mg/mL of fluorescein tetramethylrhodamine-tagged dextran (average M_r, 70 K) for 12 h and then incubated with PBS, CIT (20 μM), $PtCu_3$-PEG (100 μg/mL for $PtCu_3$), $PtCu_3$-PEG@CIT (100 μg/mL for $PtCu_3$, 20 μM for CIT) in culture media. Then, the 4% formaldehyde was utilized to fix the cells. The cells were imaged by using fluorescence microscope. The excitation of fluorescein is 488 nm and the excitation of tetramethylrhodamine is 543 nm. Emission was collected in 500–550 nm bands for fluorescein and 590–700 nm bands for tetramethylrhodamine).

2.14. In vivo studies

Female BALB/c mice (4 weeks old, 16–18 g) were purchased from Shanghai Laboratory Animal Center, and were used in accordance with the protocols approved by Ethics Committee of Sir Run Shaw Hospital. 4T1 cells was injected to the mice, the examinations were carried out when the tumors reached ~500 mm^3. The animal experiments were grouped as follows: (1) control; (2) E; (3) CIT (0.8 mM, 100 μL); (4) $PtCu_3$-PEG (4 mg/mL, 100 μL); (5) $PtCu_3$-PEG@CIT (4 mg/mL for $PtCu_3$, 0.8 mM for CIT, 100 μL); (6) $PtCu_3$-PEG (4 mg/mL, 100 μL) + E (square wave, 10 mHz, 5 mA, 10 min); (7) $PtCu_3$-PEG@CIT (4 mg/mL for $PtCu_3$, 0.8 mM for CIT, 100 μL) + E (square wave, 10 mHz, 5 mA, 10 min).

2.15. Statistical analysis

The data were analyzed by Student's-tests with a setting significance of $p < 0.05$ (*), $p < 0.01$ (**) and $p < 0.001$ (***).

3. Results and discussion

$PtCu_3$ nanoparticles were produced *via* a typical solvothermal method following the study reported previously [28], and modified with polyethylene glycol (PEG) before the loading of CIT molecules ($PtCu_3$-PEG@CIT NPs) (Fig. 2a). Representative transmission electron microscopy (TEM) image indicates $PtCu_3$ NPs show excellent dispersion with a size of ~10 nm (Fig. 2b). The high-resolution TEM (HRTEM) image presents $PtCu_3$ nanoparticles are highly crystallographic. The lattice spacings are 0.21 nm, 0.19 nm and 0.13 nm, respectively, agreeing well with the {111}, {200} and {220} facet of $PtCu_3$ NPs (Fig. 2c, d and f). The examination using X-ray energy-dispersive spectrometer (EDS) confirms Pt and Cu elements appear in the $PtCu_3$ nanoparticles, as expected (Figs. 2e and S1). After the surface modification with PEG, the hydrodynamic diameter of $PtCu_3$-PEG is ~91.3 nm (Fig. 2g), and the particles may remain stable in various media (water, PBS and RPMI-1640 cell culture medium) with similar hydrodynamic

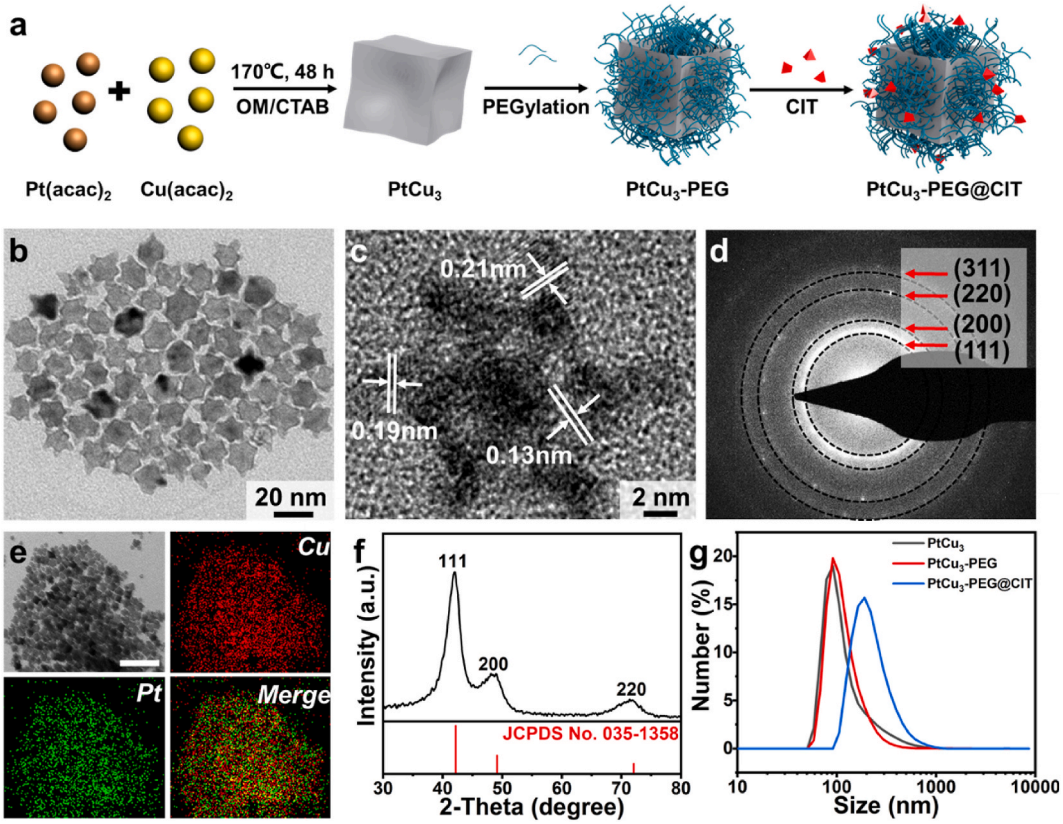

Fig. 2. Formation and representation of $PtCu_3$-PEG@CIT nanoparticles. (a) Schematic illustration of the synthetic process of $PtCu_3$-PEG@CIT nanoparticles. (b) TEM image of $PtCu_3$ nanoparticles. (c) HRTEM image of $PtCu_3$ nanoparticles. (d) SAED image of $PtCu_3$ NPs. (e) EDS mapping image of $PtCu_3$ nanoparticles (scale bar = 50 nm). (f) XRD pattern of $PtCu_3$ NPs. (g) Size of $PtCu_3$, $PtCu_3$-PEG and $PtCu_3$-PEG@CIT NPs (in water) examined by DLS.

sizes (Fig. S2), and the PEG surface modification did not induce clear changes to the microstructure of the particles (Fig. S3).

Subsequently, the assessment using TMB [30,31] was conducted to investigate the generation of •OH by $PtCu_3$-PEG NPs. TMB transforms into the oxidized TMB under the action of •OH, showing characteristic absorption peaks at 652 nm. An apparent absorption peak was observed when adding $PtCu_3$-PEG into TMB-H_2O_2 solution (pH = 6) (Fig. 3a). The absorbance of TMB at 652 nm was monitored in time-scan mode using UV–vis absorption spectroscopy in a reaction solution containing $PtCu_3$-PEG, TMB and H_2O_2 with a varied concentration (10, 20, 30, 40 mM). The characteristic absorbance increases with elevated concentration of H_2O_2, indicating increased content of •OH generated (Fig. 3b). This phenomenon indicates that $PtCu_3$-PEG NPs may serve as a Fenton-like agent for •OH induction in the acidic tumor microenvironment containing H_2O_2. However, glutathione (GSH) is highly expressed in tumor cells, suppressing the efficacy of ROS-based therapies. The functionality of $PtCu_3$-PEG NPs in GSH depletion was explored by the assay using DTNB [32]. When $PtCu_3$-PEG NPs were incubated with solution containing 1 mM GSH. The characteristic absorption at 412 nm decreased with the prolonged immersion time, indicating that $PtCu_3$--PEG NPs may effectively consume GSH, as expected (Fig. 3c).

To reveal the ROS induction of $PtCu_3$-PEG NPs under electric field, methylene blue (MB) was used as a trapping agent of ROS [33,34] and investigated by UV–vis absorption spectroscopy. The electric field was applied by a set of device containing a signal generator and a power amplifier reported previously. An alternating electric field (0.1 mHz AC) was used to avoid the dramatic pH variation nearby electrodes. The absorption at 664 nm of MB of $PtCu_3$-PEG NPs under E (10 mHz, 10 mA) showed the most intense decrease comparing to that of other sample groups (Figs. 3d and S4). With the increased concentration of $PtCu_3$-PEG nanoparticles, the MB degradation accelerated (Figs. 3e and S5). The phenomena indicate $PtCu_3$-PEG NPs can effectively induce ROS under the oscillating electric field. In addition, the MB degradation by nanoparticles was studied with the solutions containing different concentrations of chloride ion. The MB degradation was accelerated with the increase of chloride ion concentration (Figs. 3f and S6).

In addition, the raw material ratio of $Pt(acac)_2$ and $Cu(acac)_2$ was varied to synthesize PtCu and Pt_3Cu nanoparticles, as comparison. The dispersibility and homogeneity of both PtCu and Pt_3Cu particles are poor (Fig. S7). Although the properties of GSH depletion were not weakened, the Fenton reaction abilities of both samples are clearly weakened comparing to $PtCu_3$ particles. More importantly, EDT ability of both samples are significantly quenched (Figs. S8–10).

To investigate the influence of the oxidation to the properties of nanoparticles, the Fenton reaction, GSH depletion and EDT abilities of the freshly synthesized nanoparticles and the synthesized nanoparticles exposed to air for 5 days were examined (Figs. S11–13). The Fenton reaction abilities of the $PtCu_3$-PEG exposed to the air for 5 days are lower than the freshly synthesized $PtCu_3$-PEG. However, the GSH depletion abilities of the $PtCu_3$-PEG exposed to the air for 5 days were not weakened. In addition, the freshly synthesized $PtCu_3$-PEG and $PtCu_3$-PEG show the similar EDT abilities. Therefore, the oxidation of the

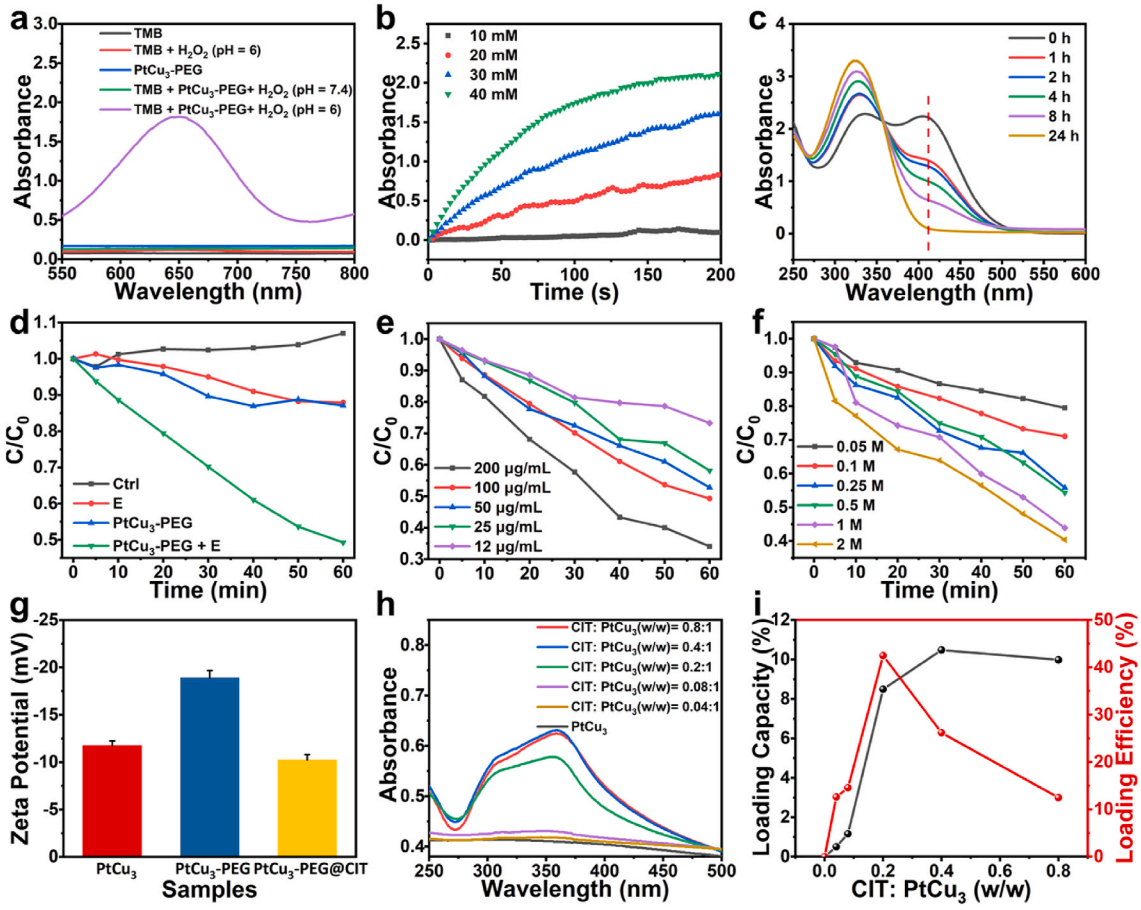

Fig. 3. Fenton reaction activity, electro-catalytic activity of $PtCu_3$-PEG and fabrication of $PtCu_3$-PEG@CIT. (a) UV–vis absorption spectrum of TMB as catalyzed by $PtCu_3$-PEG NPs with 100 mM H_2O_2 under the reaction buffer (pH = 6). (b) UV–vis absorbance at 652 nm of TMB treated with $PtCu_3$-PEG NPs at varied H_2O_2 concentrations (10, 20, 30, 40 × 10^{-3} M). (c) GSH depleting abilities of $PtCu_3$-PEG NPs. (d) MB degradation properties by $PtCu_3$-PEG NPs under E. (e) MB degradation properties by $PtCu_3$-PEG NPs at varied concentrations under E (f) MB degradation properties by $PtCu_3$-PEG NPs at varied chloride concentrations under E. (g) The zeta potential of $PtCu_3$, $PtCu_3$-PEG and $PtCu_3$-PEG@CIT NPs. (h) The UV–vis absorption spectrum of $PtCu_3$-PEG@CIT at varied mass ratios of $PtCu_3$-PEG and CIT. (i) The loading capacity and loading efficiency of CIT on $PtCu_3$-PEG NPs at different mass ratio of $PtCu_3$-PEG and CIT.

nanoparticles can weaken the Fenton reaction abilities but not the GSH depletion and EDT abilities. It is best to use the $PtCu_3$-PEG timely and avoided it exposed to the air for long time.

CIT, synthesized following the previous report [35], was verified by NMR spectra (Figs. S14–16). The zeta potentials of $PtCu_3$, $PtCu_3$-PEG and $PtCu_3$-PEG@CIT NPs were measured to be −11.76 mV, −18.9 mV and −10.24 mV (Fig. 3g), implying that CIT was successfully loaded on $PtCu_3$-PEG NPs *via* electrostatic interaction. As a result, the hydrodynamic diameter of $PtCu_3$-PEG@CIT turned to be ~190 nm (Fig. 2g). It is noteworthy that, after the loading of CIT, the microstructure of particles did not present visible variation (Fig. S17). To investigate the CIT loading efficacy, the loading procedure was carried out with different mass ratios of $PtCu_3$-PEG and CIT (CIT/$PtCu_3$ (w/w) = 0.8, 0.4, 0.2, 0.08 and 0.04). Notably, the absorption peak of CIT increased with the increased mass ratios of CIT and $PtCu_3$-PEG (Fig. 3h). The standard curve of CIT was shown in Fig. S18. According to the UV–vis absorption spectra, the loading capacity and loading efficiency of CIT on $PtCu_3$-PEG NPs were quantified (Fig. 3i). When the CIT/$PtCu_3$ ratio was set at 0.2 (w/w), the CIT loading capacity and efficiency reached ~8%wt and 45%, respectively.

In the *in vitro* assessment, normal human liver cells (7702 cells) were used to examine the cytotoxicity of as-prepared $PtCu_3$-PEG NPs. No clear negative effect was observed (Fig. 4a). In addition, no clear negative effect was induced by $PtCu_3$-PEG NPs to normal alpha mouse liver cells (AML-12 cells) (Fig. S19). The cell viability assay of 4T1 cells treated with H_2O_2 only, E only and H_2O_2 plus E group was examined, and no clear negative effects were observed (Fig. S20). When adding extra H_2O_2 (100 μM), a decreased viability of 4T1 cells appeared due to the induction of toxic •OH, and the acidic condition may further enhance the inhibition effect to cell viability (Fig. 4b**, S21**). It is noteworthy that, when the supply of electric field during the cell culture, the cell viability was further reduced, which can be attributed to the additional ROS production by EDT phenomenon.

Subsequently, the *in vitro* antitumor properties of $PtCu_3$-PEG particles before and after the integration of CIT molecules was examined and compared. 4T1 cells were co-cultured with $PtCu_3$-PEG solutions at varied concentrations of 3, 6, 12, 25, 50 μg/mL, and exposed to the treatment of AC electric field (5 mA, 10 mHz) for 3 min. As shown in Fig. 4c, the cell viabilities decreased with the increased nanoparticles dose, as expected. With prolonged treatment of electric field (5 min), an enhanced suppression effect to 4T1 cells was observed (Fig. S22). After the integration of CIT(0–50 μg/mL for $PtCu_3$ and 0–10 μM for CIT), a

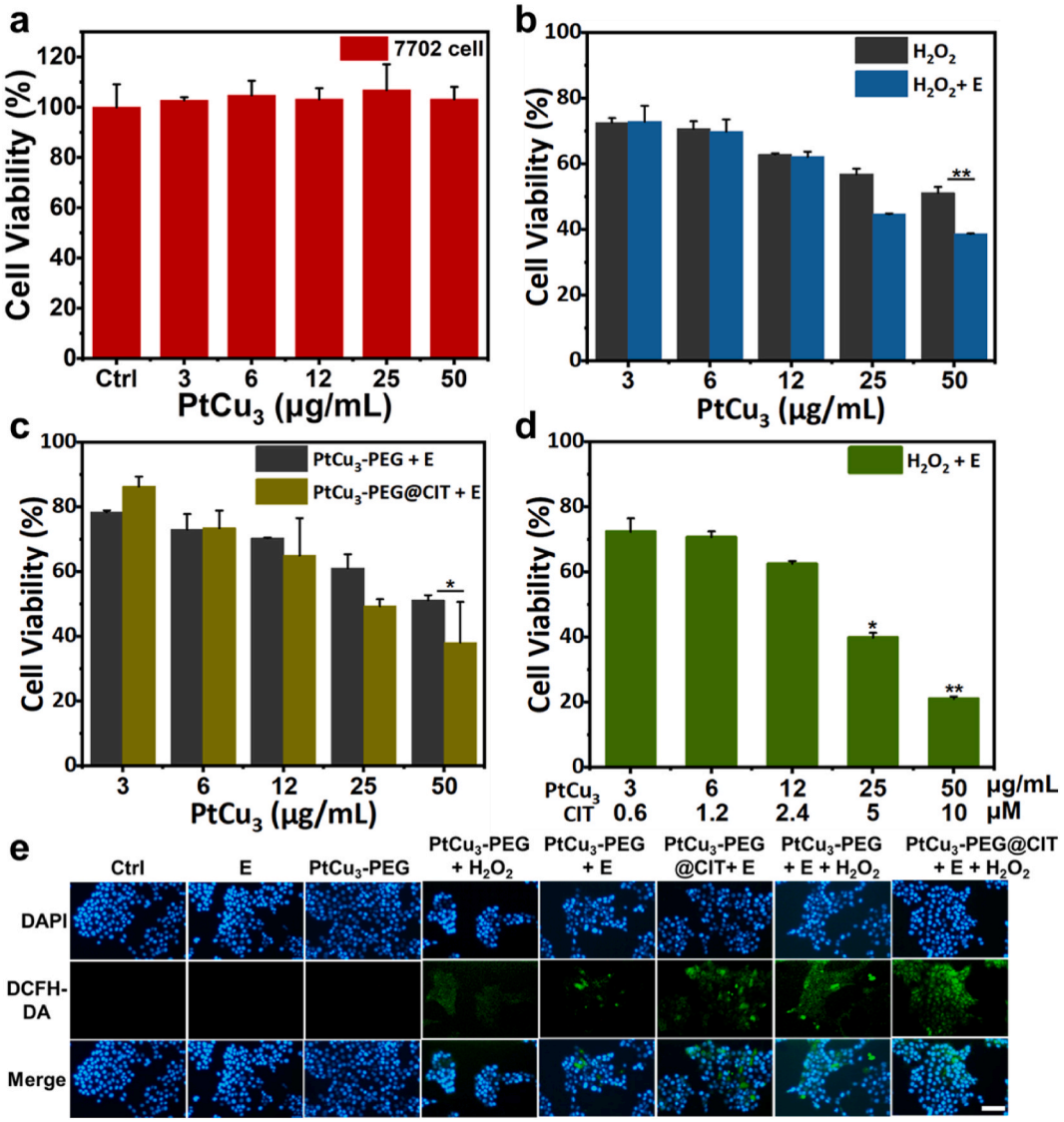

Fig. 4. In vitro study. (a) 7702 cell viability after cultured with $PtCu_3$-PEG. (b) 4T1 cell viability after cultured with $PtCu_3$-PEG NPs with H_2O_2 and with or with electric field. (c) 4T1 cell viability after cultured with $PtCu_3$-PEG and $PtCu_3$-PEG@CIT under E. (d) 4T1 cell viability after cultured with $PtCu_3$-PEG@CIT with H_2O_2 and E. (e) DCFH-DA fluorescence images to exhibit the intracellular ROS content under different condition (scale bar = 100 μm).

further reduction in cell viability occurred in the cell group using $PtCu_3$-PEG@CIT, implying the favoring role of CIT played in EDT. In addition, the cell viability of 4T1 cells, treated with $PtCu_3$-PEG@CIT (12 μg/mL for $PtCu_3$) under electric field, reduced with the increase electric current and conduction time (Fig. S23). It was also observed that the addition of extra H_2O_2 or the increased content of CIT may increase cell damage under the same condition of applied electric field (Fig. 4d). The induction of intracellular ROS after cell culture with different operations was exhibited by DCFH-DA (Figs. 4e and S24). The sample groups after single treatments, $PtCu_3$-PEG NPs, electric field (E) and H_2O_2, did not present visible fluorescence. The groups of $PtCu_3$-PEG NPs plus H_2O_2, $PtCu_3$-PEG NPs and $PtCu_3$-PEG@CIT NPs under the electric field showed weak green fluorescence. In addition, cells cultured with $PtCu_3$-PEG NPs plus H_2O_2 under the electric field and $PtCu_3$-PEG@CIT NPs under the electric field presented the enhanced fluorescence. Notably, $PtCu_3$-PEG@CIT NPs plus H_2O_2 under the electric field treatment induced the most intense green fluorescence in 4T1 cells, reflecting the highest content of ROS generated in this sample group.

To reveal the fundamental mechanism of the phenomena observed, the GSH levels in cells were investigated by DTNB. The intracellular GSH levels reduced remarkably with the increase of $PtCu_3$-PEG content, indicating that $PtCu_3$-PEG may effectively consume the intracellular

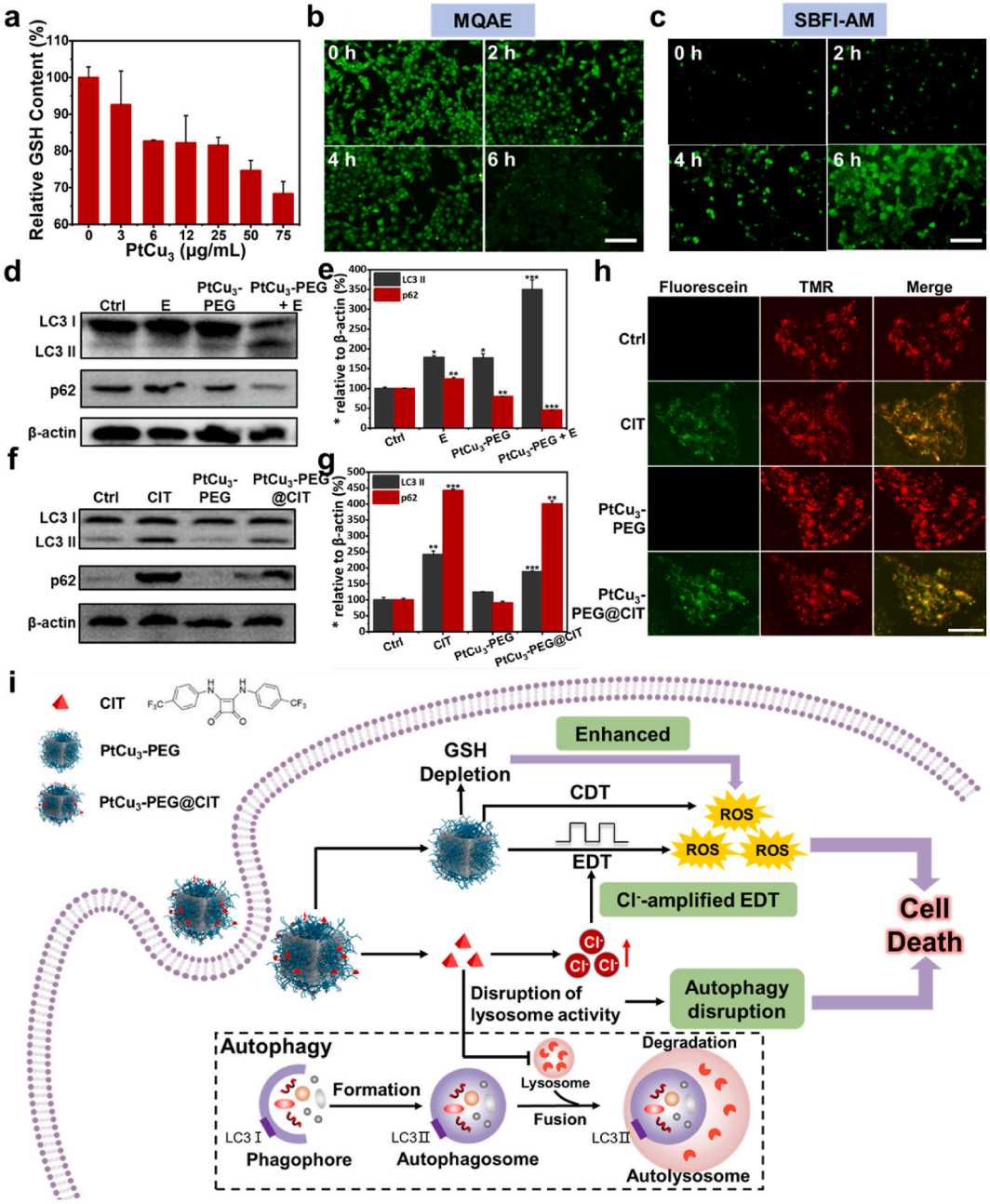

Fig. 5. Mechanism of enhanced tumor therapy by $PtCu_3$-PEG@CIT NPs. (a) Relative intracellular GSH in 4T1 cells at varied concentration of $PtCu_3$-PEG NPs. (b) Intracellular chloride ion concentration of cells after incubated with $PtCu_3$-PEG @CIT NPs for 0, 2, 4, 6 h using MQAE as probe (scale bar = 100 μm). (c) Intracellular sodium ion concentration of cells after incubated with $PtCu_3$-PEG @CIT NPs for 0, 2, 4, 6 h using SBFI-AM as probe (scale bar = 100 μm). (d and e) Western blot graph (d) and the quantitative ratio (e) of LC3 II and p62 expression level to β-actin. (f and g) Western blot graph (f) and the quantitative ratio (g) of LC3 II and p62 expression level to β-actin. (h) Fluorescent images of cells pretreated with fluorescein-tetramethylrhodamine-tagged dextran and then cultured with PBS, CIT, $PtCu_3$-PEG and $PtCu_3$-PEG@CIT for 12 h (scale bar = 50 μm). (i) Schematic illustration of $PtCu_3$-PEG@CIT NPs for CIT amplified EDT with GSH depletion. *$p < 0.05$, **$p < 0.01$ and ***$p < 0.001$ analyzed by student's t-test.

GSH (Fig. 5a). In principle, GSH is one of antioxidant for ROS clearance to protect cells from the damage by ROS. Therefore, GSH depletion could increase the intracellular ROS and induce more agitated cell damage in the ROS-based therapeutic approaches.

In addition, the Cl^- levels in cells were examined by the Cl^--quenching fluorescent probe MQAE [36]. As shown in Fig. 5b, **S25** and **S26**, the time- and concentration-dependent increase of intracellular Cl^- levels were observed after the cell incubation with $PtCu_3$-PEG@CIT. Meanwhile, the intracellular Na^+ content was examined by the sodium fluorescent probe (SBFI-AM) [37]. The time- and concentration-dependent increase of intracellular Na^+ levels occurred, well corresponding to the variation of intracellular Cl^- content (Fig. 5c, **S27** and **S28**). The findings indicate that CIT molecules function as a chloride ion transporter in conjunction with channel-mediated sodium cation co-transport. In addition, the intracellular Cl^- and Na^+ levels at different time points were quantified by Image J. The quantified fluorescence intensity of MQAE and SBFI-AM verifies the finding above (Fig. S29). In addition, 4T1 cells were incubated with CIT and $PtCu_3$-PEG@CIT in HEPES-buffered solutions, Cl^--free solutions, or Na^+-free solutions. The cell viability of CIT and $PtCu_3$-PEG@CIT had no decrease in both the Cl^--free and Na^+-free media (Figs. S30 and S31).

Autophagy is a cellular self-feeding process, protecting cells from cellular stresses and diverse therapeutics [38]. During the autophagy process, LC3 I protein on autophagosome membrane would convert to LC3 II, and examination of p62 expression has been extensively used to evaluate autophagy [39,40]. Briefly, autophagy could increase LC3-II and suppressed p62. In this study, LC3 II protein and p62 protein expression levels were investigated by Western blot assay. It could be observed that LC3 II protein content was enhanced, and p62 protein was remarkably suppressed after co-cultured with $PtCu_3$-PEG NPs under E (Fig. 5d and e). In addition, the LC3 levels of 4T1 cells after different treatments were examined by immunofluorescence (Fig. S32). Bright green fluorescence can only be observed in the groups of $PtCu_3$-PEG under the electric field, rather than the groups of $PtCu_3$-PEG or E. In addition, the autophagy levels of 4T1 cells with different treatments were also examined by autophagy detection kit (Dansylcadaverine, MDC), a type of eosinophilic stain that can stain the acidic vesicles including autophagosome within the cells (Fig. S33). In the groups of $PtCu_3$-PEG plus E, the increased bright green regions were observed comparing to other groups. The findings indicate that the EDT process could also induce autophagy of tumor cells *via* the production and effect of ROS. This reflects that the EDT process could induce clear cellular autophagy. In addition, the LC3 II protein and p62 protein levels were investigated after cell incubation with CIT and $PtCu_3$-PEG@CIT. Both cell groups presented higher expression of both LC3 II protein and p62 protein comparing to untreated cells (Ctrl) (Fig. 5f and g). The findings imply that the intracellular delivery of CIT molecules could disrupt autophagy behavior. However, LC3 I still converted to LC3 II, as the disrupted autophagy by CIT follows downstream pathway. In general, the autophagy process includes four steps, phagophore formation, autophagosome formation, autolysosome formation by fusion with lysosomes and degradation. LC3 I converted to LC3 II during autophagosome formation process. However, CIT may disrupt the function lysosome, after LC3 I converting to LC3 II, by varying the chloride ion concentration. Therefore, the LC3 II levels still increased even though CIT could disrupt autophagy. The 4T1 cells, pretreated with fluorescein-tetramethylrhodamine-tagged dextran (a lysosomal pH indicator) [41], were co-cultured with control, CIT, $PtCu_3$-PEG and $PtCu_3$-PEG@CIT (Fig. 5h). The fluorescein is dependent to pH, and it shows green fluorescence at a high pH. The tetramethylrhodamine is independent to pH, showing red fluorescence. Treatments with CIT and $PtCu_3$-PEG@CIT lead to intense green fluorescence, indicating the increase of lysosomal pH. Therefore, it is clear that in this study CIT could disrupt autophagy by disrupting the function of lysosome.

Overall, in this study, $PtCu_3$-PEG@CIT NPs may effectively induce ROS following both EDT and CDT processes. The intracellular GSH can be depleted by the particles, maintaining the high content of ROS produced. More importantly, the CIT integrated could increase intracellular chloride ion concentration, which in turn amplifies the ROS generation by the particles under the electric field. Meanwhile, the increased intracellular Cl^- concentration leads to autophagy disruption by increasing the lysosomal pH, weakening the cellular resistance to ROS. Therefore, due to the combined characteristics offered by $PtCu_3$-PEG@CIT NPs, the significant inhibition effect to tumor cells is enabled. (Fig. 5i).

In the in vivo biosafety assessment, mice bearing 4T1 tumors were intravenously (i.v.) injected with $PtCu_3$-PEG@CIT NPs. The organs and tumor were harvested after 24 h. The accumulated amount of Pt in the tumors was 1.5% of the injection dose (Fig. S34), which is higher than a variety of nanoparticles reported previously (~0.7%) [42]. This accumulation of Pt at the tumor site indicates the effective tumor accumulation of nanoparticles *via* EPR. Quantitative biodistribution data confirmed that $PtCu_3$-PEG NPs could accumulate in tumors site after 24 h. In addition, the half-life time in the blood-circulation examination was ~2.48 h (Fig. S35).

4T1 tumor-beared female Balb/c mice were utilized for the in vivo antitumoral examination, following the treatment protocol illustrated in Fig. 6a. The experimental groups included PBS (Ctrl) (Group 1), electric field only (E) (Group 2), CIT (Group 3), $PtCu_3$-PEG NPs (Group 4), $PtCu_3$-PEG@CIT NPs (Group 5), $PtCu_3$-PEG NPs + E (Group 6) and $PtCu_3$-PEG@CIT NPs + E (Group 7). The injected 100 μl $PtCu_3$-PEG@-CIT NPs contained 4 mg/mL for $PtCu_3$ and 0.8 mM for CIT. The applied electric field (E) was maintained as set at a square-wave AC (5 mA, 10 mHz, 10 min).

The mice body weight presents no clear variations during treatments, indicating negligible system toxicity of nanoparticles (Fig. 6b). The tumor size was recorded every 2 days. The tumor volume was calculated by $width^2 \times length/2$ and normalized to the initial size (Fig. 6c). Compared to the Ctrl, E (Group 2) did not exhibit apparent suppression to tumors. The CIT alone (Group 3), $PtCu_3$-PEG injection only (Group 4) as well as $PtCu_3$-PEG@CIT injection only (Group 5) exhibited weak suppression to tumors. It is noteworthy that, comparing to the previous study using $PtCu_3$ nanoparticles for CDT-enhanced sonodynamic therapy [16], the tumor suppression of $PtCu_3$-PEG injection only was lower in this study, which may be attributed to larger initial tumor size (~500 mm^3). The tumor progress in $PtCu_3$-PEG + E (Group 6) was partially suppressed. In addition, tumor progress in Group 7 presented the most significant tumor suppression in all groups. At the end of experiment, all the tumors were harvested and weighted (Fig. 6d). As expected, the tumor from Group 7 ($PtCu_3$-PEG@CIT + E) were remarkably smaller than the other groups.

Additionally, hematoxylin and eosin (H&E) staining, TdT-mediated dUTP Nick-End Labeling (TUNEL) staining and immunohistochemistry Ki-67 staining of tumor section evidenced that tumor in Group 7 presented more intense apoptosis and reduced cell proliferation (Fig. 6e–g and **S36**). The blood routine indices of mice injected with $PtCu_3$-PEG@CIT exhibited no significant changes compared to the control (Fig. S37), and no morphological variations in H&E staining images of different organs were observed (Fig. S38), implying the particles do not induce clear long-term toxicity.

The in vivo ROS content was examined by the DCFH-DA assay (Fig. S39). It was found that $PtCu_3$-PEG, $PtCu_3$-PEG@CIT and $PtCu_3$-PEG + E could improve ROS levels, while the highest ROS level was induced in the group of $PtCu_3$-PEG@CIT + E. In order to reveal the efficacy of CIT in tumor inhibition, the tumors of different treatment groups were collected at 24 h post treatment for the assessments of chloride ion concentration, lysosomal pH and LC3 levels staining (Fig. S40). It was found that tumors in Group 3, 5, 7 presented more cytosolic chloride concentrations, increased lysosomal pH and higher LC3 levels, reflecting the in vivo efficacy of CIT and $PtCu_3$-PEG@CIT. The higher LC3 levels is attributed that CIT disrupts the autophagy by increasing the lysosomal pH, and thus inhibits the degradation of LC3 II.

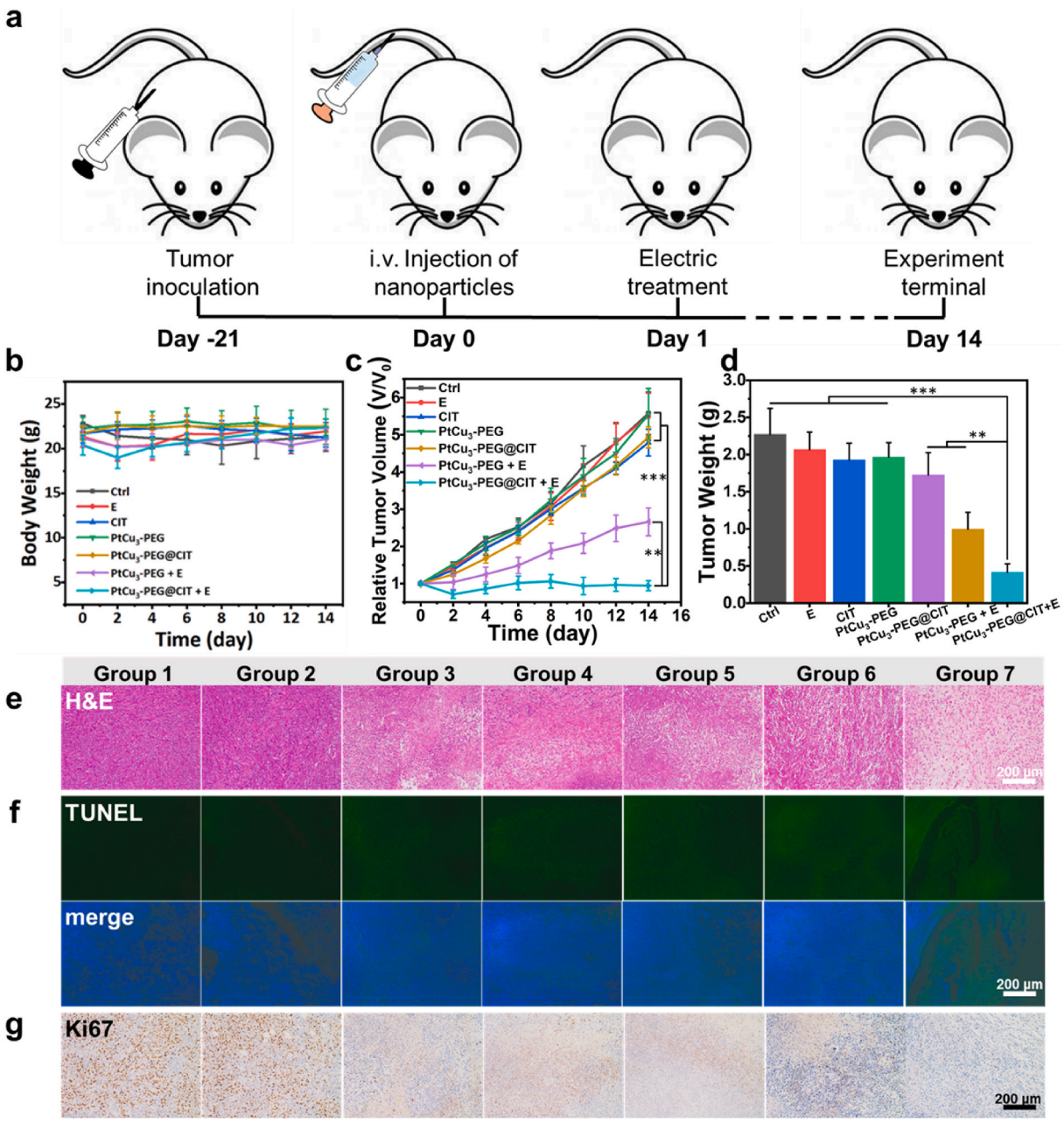

Fig. 6. In vivo study. (a) Schematic illustration of treatment process in vivo. (b) Average body weights of mice after different treatments. (c) Normalized tumor volume of different groups compared to the initial tumor volume. (d) The tumor weights harvested at the end of experiment. (e) Microscopic H&E images. (f) Immunofluorescence TUNEL images. (g) Immunofluorescence Ki67 images of stained tumor slices of different groups. (*p < 0.05, **p < 0.01 and ***p < 0.001 analyzed by student's t-test).

In addition, the in vivo anti-tumor effect of Ctrl, CIT + E, $PtCu_3$-PEG + CIT and $PtCu_3$-PEG + CIT + E were investigated (Fig. S41). Compared to the Ctrl group, CIT + E and $PtCu_3$-PEG + CIT did not exhibit clear suppression to tumors, while $PtCu_3$-PEG + CIT + E presented the tendency to grow continually. However, $PtCu_3$-PEG@CIT + E in Fig. 6c presents the most significant tumor suppression. Therefore, it turns out that $PtCu_3$-PEG@CIT + E shows promoted tumor inhibition than $PtCu_3$-PEG + CIT + E.

4. Conclusions

In this study, we have designed and constructed an electric-driven combinational therapeutic platform based on fine platinum-copper alloy nanoparticles integrated with CIT molecules ($PtCu_3$-PEG@CIT NPs). The particles showed several unique characteristics: (a) intrinsic ROS generation properties as an electrosensitizer; (b) the induction of •OH at tumor microenvironment; (c) GSH depletion; (d) increased intracellular chloride ion concentration to promote electric-driven ROS generation; (e) lysosome disruption to suppress autophagy by increase lysosomal pH. Due to the effective integration of diverse functionalities, $PtCu_3$-PEG@CIT NPs exhibit excellent anti-tumor property *in vitro* and in vivo, to tumors with relatively large initial sizes (~500 mm^3) under the oscillating electric field. This study appears to offer a distinctive concept in enhancing the antitumor efficacy of EDT following the current mechanism understanding of this technology in cancer treatment.

CRediT authorship contribution statement

Tong Chen: Methodology, Software, Validation, Formal analysis, Investigation, Resources, Data curation, Writing – original draft. **Gaorong Han:** Supervision. **Xiang Li:** Conceptualization, Supervision, Writing – review & editing.

Declaration of competing interest

The authors declare no conflict of interest.

Acknowledgments

This work was financially supported by National Natural Science Foundation of China (52172289), Provincial Key research program of Zhejiang Province (2020C04005), '111' Program funded by Education Ministry of China and Sate Bureau of Foreign Experts Affairs (B16043) and Fundamental Research Funds for the Central Universities of China.

Appendix A. Supplementary data

Supplementary data to this article can be found online at https://doi.org/10.1016/j.bioactmat.2021.10.012.

References

[1] T. Gu, Y. Wang, Y. Lu, L. Cheng, L. Feng, H. Zhang, X. Li, G. Han, Z. Liu, Platinum nanoparticles to enable electrodynamic therapy for effective cancer treatment, Adv. Mater. 31 (14) (2019) 1806803.
[2] T. Chen, T. Gu, L. Cheng, X. Li, G. Han, Z. Liu, Porous Pt nanoparticles loaded with doxorubicin to enable synergistic Chemo-/Electrodynamic Therapy, Biomaterials 255 (2020) 120202.
[3] Z. Lu, J. Gao, C. Fang, Y. Zhou, X. Li, G. Han, Porous Pt nanospheres incorporated with GOx to enable synergistic oxygen-inductive starvation/electrodynamic tumor therapy, Adv. Sci. 7 (17) (2020) 2001223.
[4] T. Gu, T. Chen, L. Cheng, X. Li, G. Han, Z. Liu, Mesoporous silica decorated with platinum nanoparticles for drug delivery and synergistic electrodynamic-chemotherapy, Nano Research 13 (8) (2020) 2209–2215.
[5] Y. Raju, P. Krishnamurthi, P.L. Pauloseb, P.T. Manoharan, Substrate-free copper nanoclusters exhibit super diamagnetism and surface based soft ferromagnetism, Nanoscale 9 (2017) 17963–17974.
[6] J. Bornacelli, C. Torres-Torres, J. Arenas-Alatorre, M.M. Martínez-Mondragón, L. Rodríguez-Fernández, A. Oliver, Enhanced ultrafast optomagnetic effects in room-temperature ferromagnetic Pt nanoclusters embedded in silica by ion implantation, Nanotechnology 31 (2020) 355705.
[7] T. Stauber, T.J. Jentsch, Chloride in vesicular trafficking and function, Annu. Rev. Physiol. 75 (2013) 453–477.
[8] N. Busschaert, S.H. Park, K.H. Baek, Y.P. Choi, J. Park, E.N.W. Howe, J.R. Hiscock, L.E. Karagiannidis, I. Marques, V. Felix, W. Namkung, J.L. Sessler, P.A. Gale, I. Shin, A synthetic ion transporter that disrupts autophagy and induces apoptosis by perturbing cellular chloride concentrations, Nat. Chem. 9 (7) (2017) 667–675.
[9] M.S. Melvin, J.T. Tomlinson, G.R. Saluta, G.L. Kucera, N. Lindquist, R. A. Manderville, Double-strand DNA cleavage by copper prodigiosin, J. Am. Chem. Soc. 122 (26) (2000) 6333–6334.
[10] J.L. Sessler, L.R. Eller, W.S. Cho, S. Nicolaou, A. Aguilar, J.T. Lee, V.M. Lynch, D. J. Magda, Synthesis, anion-binding properties, and in vitro anticancer activity of prodigiosin analogues, Angew. Chem. Int. Ed. 44 (37) (2005) 5989–5992.
[11] T. Sato, H. Konno, Y. Tanaka, T. Kataoka, K. Nagai, H.H. Wasserman, S. Ohkuma, Prodigiosins as a new group of H+/Cl- symporters that uncouple proton translocators, J. Biol. Chem. 273 (34) (1998) 21455–21462.
[12] P.A. Gale, M.E. Light, B. McNally, K. Navakhun, K.E. Sliwinski, B.D. Smith, Co-transport of H^+/Cl^- by a synthetic prodigiosin mimic, Chem. Commun. 30 (2005) 3773–3775.
[13] N. Busschaert, I.L. Kirby, S. Young, S.J. Coles, P.N. Horton, M.E. Light, P.A. Gale, Squaramides as potent transmembrane anion transporters, Angew. Chem. Int. Ed. 51 (18) (2012) 4426–4430.
[14] S. Hosogi, K. Kusuzaki, T. Inui, X. Wang, Y. Marunaka, Cytosolic chloride ion is a key factor in lysosomal acidification and function of autophagy in human gastric cancer cell, J. Cell Mol. Med. 18 (2014) 1124–1133.
[15] T. Stauber, T.J. Jentsch, Chloride in vesicular trafficking and function, Annu. Rev. Physiol. 75 (2013) 453–477.
[16] N. Mizushima, M. Komatsu, Autophagy: renovation of cells and tissues, Cell 147 (4) (2011) 728–741.
[17] B.E. García-Pérez, J.A. González-Rojas, M.I. Salazar, C. Torres-Torres, N. S. Castrejón-Jiménez, Taming the autophagy as a strategy for treating COVID-19, Cells 9 (12) (2020) 2679.
[18] V. Catalano, A. Turdo, S. Di Franco, F. Dieli, M. Todaro, G, Tumor and its microenvironment: a synergistic interplay. Stassi, Semin. Cancer Biol. 23 (6) (2013) 522–532.
[19] Z.L. Dong, L.Z. Feng, Y. Chao, Y. Hao, M.C. Chen, F. Gong, X. Han, R. Zhang, L. Cheng, Z. Liu, Amplification of tumor oxidative stresses with liposomal Fenton catalyst and glutathione inhibitor for enhanced cancer chemotherapy and radiotherapy, Nano Lett. 19 (2) (2019) 805–815.
[20] F. Gong, L. Cheng, N.L. Yang, Q.T. Jin, L.L. Tian, M.Y. Wang, Y.G. Li, Z. Liu, Bimetallic oxide MnMoOx nanorods for in vivo photoacoustic imaging of GSH and tumor-specific photothermal therapy, Nano Lett. 18 (9) (2018) 6037–6044.
[21] S. Wang, F. Li, R. Qiao, X. Hu, H. Liao, L. Chen, J. Wu, H. Wu, M. Zhao, J. Liu, R. Chen, X. Ma, D. Kim, J. Sun, T.P. Davis, C. Chen, J. Tian, T. Hyeon, D. Ling, Arginine-rich manganese silicate nanobubbles as a ferroptosis-inducing agent for tumor-targeted theranostics, ACS Nano 12 (12) (2018) 12380–12392.
[22] X. Jing, Y. Xu, D. Liu, Y. Wu, N. Zhou, D. Wang, K. Yan, L. Meng, Intelligent nanoflowers: a full tumor microenvironment-responsive multimodal cancer theranostic nanoplatform, Nanoscale 11 (33) (2019) 15508–15518.
[23] Y. Huang, Y. Jiang, Z. Xiao, Y. Shen, L. Huang, X. Xu, G. Wei, C. Xu, C. Zhao, Three birds with one stone: a ferric pyrophosphate based nanoagent for synergetic NIR-triggered photo/chemodynamic therapy with glutathione depletion, Chem. Eng. J. 380 (2020) 122369.
[24] X. Wan, H. Zhong, W. Pan, Y. Li, Y. Chen, N. Li, B. Tang, Programmed release of dihydroartemisinin for synergistic cancer therapy using a CaCO3 mineralized metal-organic framework, Angew. Chem. Int. Ed. 58 (40) (2019) 14134–14139.
[25] C. Wang, F. Cao, Y. Ruan, X. Jia, W. Zhen, X. Jiang, Specific generation of singlet oxygen through the russell mechanism in hypoxic tumors and GSH depletion by Cu-TCPP nanosheets for cancer therapy, Angew. Chem. Int. Ed. 58 (29) (2019) 9846–9850.
[26] Y. Liu, J. Wu, Y. Jin, W. Zhen, Y. Wang, J. Liu, L. Jin, S. Zhang, Y. Zhao, S. Song, Y. Yang, H. Zhang, Copper(I) phosphide nanocrystals for in situ self-generation magnetic resonance imaging-guided photothermal-enhanced chemodynamic synergetic therapy resisting deep-seated tumor, Adv. Funct. Mater. 29 (50) (2019) 1904678.
[27] F. Gong, L. Cheng, N. Yang, O. Betzer, L. Feng, Q. Zhou, Y. Li, R. Chen, R. Popovtzer, Z. Liu, Ultrasmall oxygen-deficient bimetallic oxide $MnWO_X$ nanoparticles for depletion of endogenous GSH and enhanced sonodynamic cancer therapy, Adv. Mater. 31 (23) (2019) 1900730.
[28] X. Zhong, X. Wang, L. Cheng, Y. Tang, G. Zhan, F. Gong, R. Zhang, J. Hu, Z. Liu, X. Yang, GSH-Depleted $PtCu_3$ nanocages for chemodynamic-enhanced sonodynamic cancer therapy, Adv. Funct. Mater. 30 (4) (2019) 1907954.
[29] J. Li, X. Zu, G. Liang, K. Zhang, Y. Liu, K. Li, Z. Luo, K. Cai, Octopod PtCu nanoframe for dual-modal imaging-guided synergistic photothermal radiotherapy, Theranostics 8 (4) (2018) 1042–1058.
[30] M. Huo, L. Wang, Y. Chen, J. Shi, Tumor-selective catalytic nanomedicine by nanocatalyst delivery, Nat. Commun. 8 (1) (2017) 357.
[31] S. Gao, H. Lin, H. Zhang, H. Yao, Y. Chen, J. Shi, Nanocatalytic tumor therapy by biomimetic dual inorganic nanozyme-catalyzed cascade reaction, Adv. Sci. 6 (3) (2019) 1801733.
[32] X. Nie, L. Xia, H.L. Wang, G. Chen, B. Wu, T.Y. Zeng, C.Y. Hong, L.H. Wang, Y. Z. You, Photothermal therapy nanomaterials boosting transformation of Fe(III) into Fe(II) in tumor cells for highly improving chemodynamic therapy, ACS Appl. Mater. Interfaces 11 (35) (2019) 31735–31742.
[33] J.S. Lee, K.H. You, C.B. Park, Highly photoactive, low bandgap TiO_2 nanoparticles wrapped by graphene, Adv. Mater. 24 (8) (2012) 1084–1088.
[34] Y.N. Tang, W.H. Di, X.S. Zhai, R.Y. Yang, W.P. Qin, NIR-responsive photocatalytic activity and mechanism of NaYF4:Yb,Tm@TiO2 core-shell nanoparticles, ACS Catal. 3 (3) (2013) 405–412.
[35] S.K. Ko, S.K. Kim, A. Share, V.M. Lynch, J. Park, W. Namkung, W. Van Rossom, N. Busschaert, P.A. Gale, J.L. Sessler, I. Shin, Synthetic ion transporters can induce apoptosis by facilitating chloride anion transport into cells, Nat. Chem. 6 (10) (2014) 885–892.
[36] H.J. Cho, H.Y. Gee, K.H. Baek, S.K. Ko, J.M. Park, H. Lee, N.D. Kim, M.G. Lee, I. Shin, A small molecule that binds to an ATPase domain of Hsc70 promotes membrane trafficking of mutant cystic fibrosis transmembrane conductance regulator, J. Am. Chem. Soc. 133 (50) (2011) 20267–20276.
[37] W. Jiang, L. Yin, H. Chen, A.V. Paschall, L. Zhang, W. Fu, W. Zhang, T. Todd, K. S. Yu, S. Zhou, Z. Zhen, M. Butler, L. Yao, F. Zhang, Y. Shen, Z. Li, A. Yin, H. Yin, X. Wang, F.Y. Avci, X. Yu, J. Xie, NaCl nanoparticles as a cancer therapeutic, Adv. Mater. 31 (46) (2019) 1904058.
[38] A. Kuma, M. Matsui, N. Mizushima, LC3, an autophagosome marker, can be incorporated into protein aggregates independent of autophagy, Autophagy 3 (4) (2007) 323–328.
[39] X. Ren, Y. Chen, H. Peng, X. Fang, X. Zhang, Q. Chen, X. Wang, W. Yang, X. Sha, Blocking autophagic flux enhances iron oxide nanoparticle photothermal therapeutic efficiency in cancer treatment, ACS Appl. Mater. Interfaces 10 (33) (2018) 27701–27711.
[40] X. Wu, Y. Wu, Z. Wang, L. Liu, C. Sun, Y. Chen, C. Wang, A cascade-targeting nanocapsule for enhanced photothermal tumor therapy with aid of autophagy inhibition, Adv. Health. Mater. 7 (11) (2018) 1800121.
[41] J.E. DiCiccio, B.E. Steinberg, Lysosomal pH and analysis of the counter ion pathways that support acidification, J. Gen. Physiol. 137 (4) (2011) 385–390.
[42] S. Wilhelm, A.J. Tavares, Q. Dai, S. Ohta, J. Audet, H.F. Dvorak, W.C.W. Chan, Analysis of nanoparticle delivery to tumours, Nat. Rev. Mater. 1 (5) (2016) 16014.